



Title	Rotating Stratified Barotropic Flow over Topography : Mechanisms of the Cold Belt Formation off the Soya Warm Current along the Northeastern Coast of Hokkaido
Author(s)	Mitsudera, Humio; Uchimoto, Keisuke; Nakamura, Tomohiro
Citation	Journal of Physical Oceanography, 41(11), 2120-2136 <a href="https://doi.org/10.1175/2011JPO4598.1">https://doi.org/10.1175/2011JPO4598.1</a>
Issue Date	2011-11
Doc URL	<a href="http://hdl.handle.net/2115/49113">http://hdl.handle.net/2115/49113</a>
Rights	© Copyright 2011 American Meteorological Society (AMS). Permission to use figures, tables, and brief excerpts from this work in scientific and educational works is hereby granted provided that the source is acknowledged. Any use of material in this work that is determined to be "fair use" under Section 107 of the U.S. Copyright Act or that satisfies the conditions specified in Section 108 of the U.S. Copyright Act (17 USC § 108, as revised by P.L. 94-553) does not require the AMS' s permission. Republication, systematic reproduction, posting in electronic form, such as on a web site or in a searchable database, or other uses of this material, except as exempted by the above statement, requires written permission or a license from the AMS. Additional details are provided in the AMS Copyright Policy, available on the AMS Web site located at ( <a href="http://www.ametsoc.org/">http://www.ametsoc.org/</a> ) or from the AMS at 617-227-2425 or <a href="mailto:copyright@ametsoc.org">copyright@ametsoc.org</a> .
Type	article
File Information	JPO41-11_2120-2136.pdf



[Instructions for use](#)

# Rotating Stratified Barotropic Flow over Topography: Mechanisms of the Cold Belt Formation off the Soya Warm Current along the Northeastern Coast of Hokkaido

HUMIO MITSUDERA, KEISUKE UCHIMOTO, AND TOMOHIRO NAKAMURA

*Institute of Low Temperature Science, Hokkaido University, Sapporo, Japan*

(Manuscript received 7 October 2010, in final form 12 April 2011)

## ABSTRACT

The Soya “Warm Current” (SWC) flows through a shallow strait between the Japan Sea and the Sea of Okhotsk. The SWC has a jet structure downstream of the strait along the northern coast of Hokkaido with a maximum speed exceeding  $1 \text{ m s}^{-1}$  at its axis in summer and fall. A surface cold belt with a subsurface doming structure forms offshore of the SWC axis. Mechanisms of the cold belt formation are discussed from a point of view of resonant interaction between a barotropic stratified flow and a shallow sill and subsequent baroclinic adjustment along the SWC. When a stratified current rides a slope upstream, the thermocline displaces upward greatly and outcrops owing to resonant generation of internal Kelvin waves if the upper layer is thinner than the lower layer. The control section, where a Froude number is unity, occurs “upstream” from the sill crest when the ambient inflow has a barotropic flow component. These upwelling features closely resemble those along the southwestern coast of Sakhalin Island. The SWC then flips from an upwelling-type to a downwelling-type structure; in doing so, it transits from the west coast of Sakhalin to the east coast of Hokkaido. It is this transition that leads to the offshore doming structure, which propagates downstream as a vorticity wave, manifesting the cold belt at the surface.

## 1. Introduction

The “Soya Warm Current” (SWC) flows along the east coast of Hokkaido in the Sea of Okhotsk (Fig. 1a). It originates in the Japan Sea where the flow is broad and relatively weak. As it passes Soya Strait north of Hokkaido (see Fig. 1b), however, the current acquires a jetlike structure in summer and fall with a maximum speed exceeding  $1 \text{ m s}^{-1}$  at its axis (Ebuchi et al. 2006; Matsuyama et al. 2006; Fukamachi et al. 2008). The flow of the SWC is nearly barotropic near the coast, while a baroclinic structure becomes evident around the jet axis at about 30 km from the coast. Seasonal variations are distinct in the SWC, in which the surface current is strongest in summer while it is nearly absent in winter. The SWC is driven by the sea level difference between the Japan Sea and the Sea of Okhotsk; the basinwide wind stress distribution over the North Pacific is responsible for the mean sea level difference, while the alongshore wind in the Sea of Okhotsk is responsible for the seasonal variations (e.g., Tsujino et al. 2008).

One of characteristics of the SWC is that it accompanies a cold water belt at the surface offshore of the SWC axis along the Hokkaido coast (Fig. 1a, see also Matsuyama et al. 2006; Ishizu et al. 2006, and references therein). The cold belt is apparently generated along the southwestern coast of Sakhalin Island upstream of the strait and extends southward along the SWC. Further, a subsurface doming structure develops below the surface cold belt, as shown in Ishizu et al. (2006). Therefore, subsurface cold water outcrops to form the surface cold belt. This cold belt tends to exist throughout summer and fall, which is important for biological production in the region (Mustapha et al. 2009). We note that it is not likely to be driven by wind because the mean wind stress is weak in summer ( $<0.01 \text{ N m}^{-2}$ ).

In this paper, we investigate the formation of the cold water belt from a point of view of hydraulics at Soya Strait, which is shallow with a depth of 50 m, and subsequent baroclinic wave adjustment downstream along the SWC. The cold belt forms offshore of the SWC during summer when the current is strongest (Ebuchi et al. 2006; Fukamachi et al. 2008), incorporating a substantial barotropic component (e.g., Matsuyama et al. 2006). Further, a shallow seasonal thermocline is present at a depth of  $\sim 30 \text{ m}$  in the Japan Sea where the current

*Corresponding author address:* Humio Mitsudera, Institute of Low Temperature Science, Hokkaido University, Nishi-8, Kita-19, Sapporo 060-0819, Japan.  
E-mail: humiom@lowtem.hokudai.ac.jp

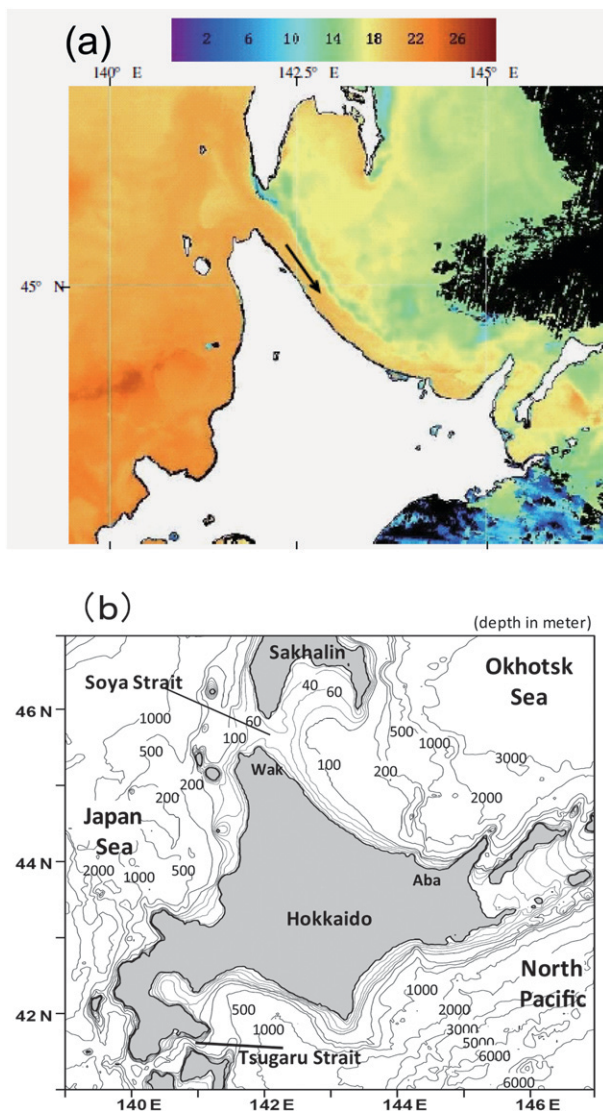


FIG. 1. (a) Satellite image on 21 Aug 2001 showing the Soya warm current (SWC) and the surface cold belt offshore. The black arrow indicates the SWC (adopted from Ishizu et al. 2006). (b) Bottom topography and geometry around Hokkaido Island.

originates. Hydraulic control associated with the SWC occurs if a long wave, whose phase speed is close to zero with respect to topography, exists in such a flow configuration. One of the candidates is an internal Kelvin wave along the Sakhalin coast because it propagates against the SWC with a phase speed  $O(1 \text{ m s}^{-1})$  relative to the current. As seen later, shoaling of the thermocline near the Sakhalin coast is likely to occur owing to generation of internal Kelvin waves forced by a stratified barotropic flow interacting with topography.

Baroclinic response of a stratified barotropic flow to topographic forcings was considered first by Pratt and Armi (1990) for a contracting lateral-wall geometry with a

flat bottom. They found that, in addition to usual controls at topographic extremes such as minimum widths, points of control may also occur remotely from the extreme when a net depth-integrated throughflow is present. They called this control the “remote control.” We will show that the remote control causes upwelling in response to bottom topographic forcing, providing as the thermocline is shallow, using a two-layer analytical model (section 2) and numerical experiments of a simple channel model (section 3). As seen in Fig. 1a, the cold belt originates off the southwestern Sakhalin coast apparently, which is upstream from the shallowest part of Soya Strait, suggesting that upwelling would take place by the remote control.

The surface cold belt and the subsurface thermocline shoaling develop downstream subsequently along the SWC off the coast of Hokkaido. The mechanism of the downstream development is another subject to be discussed in the present study. As noted before, this is not generated merely by advection of the cold surface water from upstream, but by outcropping of cold water from below. Ishizu et al. (2006) suggested that the cold water upwells due to the Ekman pumping from the bottom boundary layer associated with cyclonic vorticity between the nearshore strong current and offshore calm water. However, stratification over the sloping bottom may shut down Ekman pumping due to the thermal wind balance within a few days after spinup of the overlying current (Chapman 2002). It is doubtful, therefore, whether Ekman pumping remains strong enough to pump the cold water up to the surface. In this paper, instead, the subsurface doming is shown to be a consequence of adjustment by baroclinic waves that propagate downstream from the upwelling region (section 3).

In the remainder of this section, we will describe results of a realistic general circulation model (GCM) by Uchimoto et al. (2007), which represents the SWC and the cold belt quite realistically (henceforth referred to as the Okhotsk GCM). It is useful to observe the realistic model results to extract dynamical essences of the cold belt formation because current measurements are limited in reality, and even hydrographic measurements are nearly absent along the Sakhalin coast.

The Okhotsk GCM is a part of the model developed for the Japan Coastal Ocean Predictability Experiment (JCOPE) (e.g., Miyazawa et al. 2008), based on a general coordinate version of the Princeton Ocean Model (POM) (Mellor et al. 2002). The resolution of the Okhotsk GCM is  $1/12^\circ$  with the domain from  $40^\circ$  to  $62^\circ\text{N}$ ,  $135^\circ$  to  $165^\circ\text{E}$  covering the entire Sea of Okhotsk. Detailed description of the model was given in Uchimoto et al. (2007).

Figure 2a displays SST and a depth-averaged (barotropic) flow along the Okhotsk coast of Hokkaido reproduced in the Okhotsk GCM. The surface cold belt

offshore of the SWC is represented quite well in the simulation, although it is marginally resolved since the Okhotsk GCM has  $1/12^\circ$  resolution. Temperature difference between the cold belt and SWC water is typically  $\sim 2^\circ\text{C}$ , somewhat weaker than that in reality. The SWC is strengthened as it flows over a sill topography in the strait and becomes a jetlike flow along Hokkaido Island. There is also a coastal flow along the west coast of Sakhalin. A smooth transition of the SWC from the Sakhalin coast to the Hokkaido coast is likely a result of adjustment by shelf waves, as discussed in Ohshima (1994), responding to a sea level difference between the Japan Sea and Sea of Okhotsk. Net transport of the SWC is 0.8 Sv ( $\text{Sv} \equiv 10^6 \text{ m}^3 \text{ s}^{-1}$ ) in summer in this model, which is comparable with (but smaller than) the observed transport (e.g., Ebuchi et al. 2006). Depth-averaged speed is typically  $0.6 \text{ m s}^{-1}$  in the strait.

Cross sections of potential temperature off Sakhalin and Hokkaido are displayed in Figs. 2b and 2c, respectively. On the Okhotsk coast of Hokkaido (Fig. 2c), SWC water warmer than  $18^\circ\text{C}$  flows along the coast. There is a sharp decrease of potential temperature to  $5^\circ\text{C}$ , which is the Okhotsk water, resembling observations. The current axis is present at this temperature transition zone with strong vertical and horizontal shear. The cold water offshore of the axis shows a doming structure and the thermocline water ( $\sim 15^\circ\text{C}$ ) outcrops to the surface at about  $143.3^\circ\text{E}$ , consistent with observations (see, e.g., Ishizu et al. 2006).

Potential temperature upstream from the strait is shown in Fig. 2b. The seasonal thermocline is seen at a depth of  $\sim 30 \text{ m}$ . The thermocline shoals toward the Sakhalin coast, manifesting an upwelling structure. A typical horizontal scale of the upwelling is  $\sim 10 \text{ km}$  in the offshore direction, which is characterized by the internal Rossby radius. Therefore, the upwelling structure is likely to be caused by internal Kelvin waves along the Sakhalin coast. Published observations in this region are extremely limited. An exceptional observation was presented by Nakata et al. (1996) in which the shallow seasonal thermocline and upwelling structure with a scale of baroclinic Rossby radius was clearly observed.

The above numerical results suggest that dynamics of the cold belt formation should be characterized by a shallow sill, a net depth-averaged (barotropic) throughflow, and ambient shallow stratification corresponding to the seasonal thermocline. In the following sections, we consider a rotating channel model in which a barotropic stratified flow interacts with a localized sill. A model with straight coastlines is discussed here, so a topographic extreme is present at the crest of the sill. This model is simple enough to be tractable analytically (see section 2). Numerical experiments of the cold belt formation are

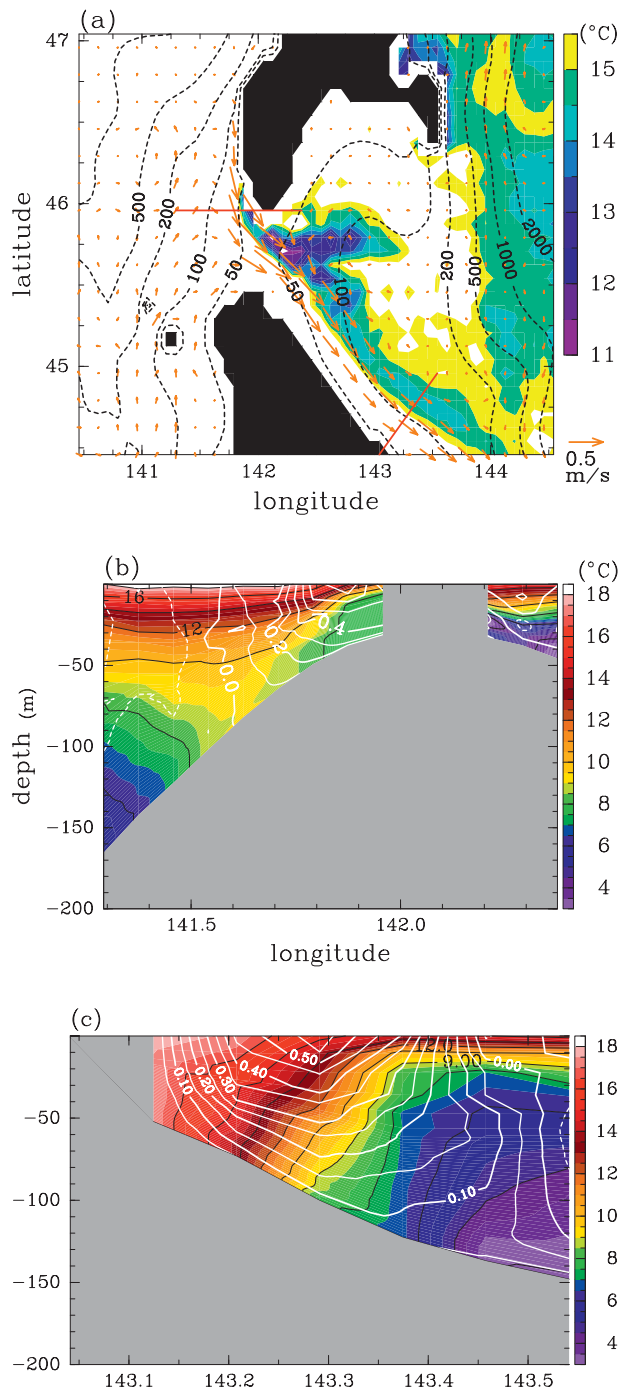


FIG. 2. (a) Surface cold belt simulated in the GCM; the monthly mean SST in August (color shade) and the depth-averaged flow field (vectors) are shown. Contours denote depths. Red lines indicate sections shown in Figs. 2b,c. (b) Cross section of potential temperature (color shade) and alongshore velocity (white contour) off the coast of south Sakhalin upstream from Soya Strait. Temperature contour interval is  $1.5^\circ\text{C}$ . Velocity contour interval is  $0.1 \text{ m s}^{-1}$  where southward flow is denoted as positive. (c) As in (b) except off the coast of Hokkaido downstream from the Soya Strait.

then discussed, using a simple model configuration in section 3 that is comparable to the analytical model. In section 4, characteristics of hydraulic solutions and comparison between the simple model and the above GCM results are briefly discussed.

## 2. Hydraulics of a barotropic stratified flow over a sill

### a. Forced nonlinear internal Kelvin waves

In this section we discuss mechanisms of intensive upwelling along the southwestern coast of Sakhalin Island using a simple channel model. We consider a straight channel with width  $L$  and bottom topography  $h(x)$  situated on an  $f$  plane, as shown in Fig. 3, where  $x$ ,  $y$ , and  $z$  denote the along-channel, cross-channel, and vertical directions, respectively;  $y = 0$  is defined at the center of the channel so that the left-hand (right hand) wall facing downstream is located at  $y = L/2$  ( $y = -L/2$ ). Although this is an  $f$ -plane model, we shall consider positive  $y$  direction as northward for convenience. Therefore, the left-hand wall is referred to as the northern wall (see Fig. 3), corresponding to the Sakhalin coast in the Soya Strait configuration. The isolated topography has maximum height  $h_m$  at  $x = 0$ , while  $h \rightarrow 0$  as  $x \rightarrow \pm\infty$ . The channel is filled with two-layer fluid whose density in each layer is  $\rho_i$  ( $i = 1, 2$ ), where the subscripts 1 and 2 represent variables of the upper and lower layers, respectively. We presume that a barotropic flow  $u_T(x, y)$  is present in the channel (Fig. 3). The configurations of the model are similar to those of Pratt and Armi (1990), although in the present model it is variable bottom topography  $h(x)$ , rather than contracting coastlines, that makes the barotropic flow field  $u_T(x, y)$  evolve along the channel.

The momentum and continuity equations become, with a semigeostrophic approximation where a long wave is considered in the along-channel direction,

$$\frac{\partial u_i}{\partial t} + u_i \frac{\partial u_i}{\partial x} + v_i \frac{\partial u_i}{\partial y} - f v_i = -\frac{\partial p_i}{\partial x \rho_0}, \quad (1)$$

$$f u_i = -\frac{\partial p_i}{\partial y \rho_0}, \quad (2)$$

and

$$\frac{\partial d_i}{\partial t} + \frac{\partial u_i d_i}{\partial x} + \frac{\partial v_i d_i}{\partial y} = 0, \quad (3)$$

where  $u_i$  and  $v_i$  represent the along-channel and cross-channel velocities respectively,  $d_i$  is thickness of each layer, and  $\rho_0$  is typical density assumed as a constant:  $p_i$  is the pressure in each layer such that

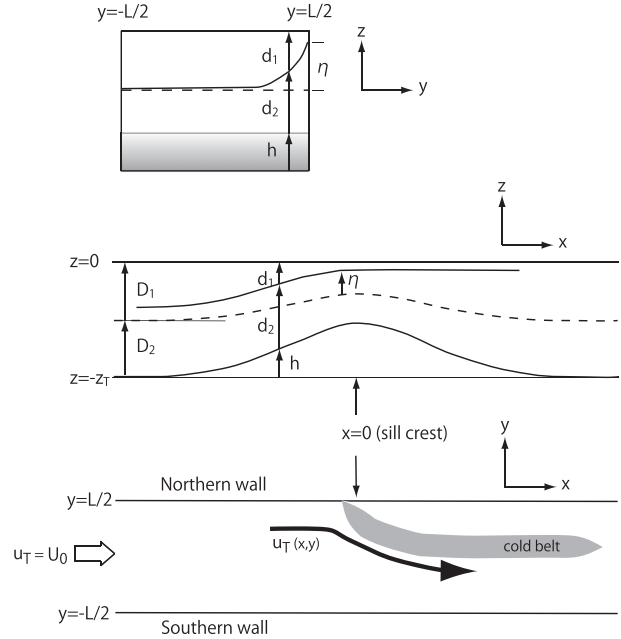


FIG. 3. Definition sketches of the present two-layer model with a sill topography: (top) cross-channel section and (middle) side view. Note that  $\eta$  is defined on the northern wall. Dashed line indicates interface position if barotropic flow would override the sill without baroclinic response. (bottom) Plan view. Net depth-averaged flow  $u_T(x, y)$  is assumed.

$$\frac{p_i}{\rho_0} = \frac{p_T}{\rho_0} + g' \delta_{i,2} (d_2 + h), \quad (4)$$

where  $p_T$  is pressure at the top where a rigid lid is assumed,  $g'$  is reduced gravity, and  $h$  is the bottom topography, as in Fig. 3. Further,  $\delta_{i,j}$  is the Kronecker delta for which  $\delta_{i,j} = 1$ , if  $i = j$ , while  $\delta_{i,j} = 0$ , otherwise.

It is assumed that potential vorticity (PV) is constant in the upper and the lower layers. As the simplest case, we assume a uniform barotropic inflow,  $u_T(-\infty, y) = U_0 = \text{const}$ , with a constant thickness in each layer,  $D_i$  ( $i = 1, 2$ ), to be imposed far upstream where  $h \rightarrow 0$ . We thus obtain

$$\frac{1}{d_i} \left( f - \frac{\partial u_i}{\partial y} \right) = \frac{f}{D_i} \quad (5)$$

from PV conservation with the semigeostrophic approximation. Equations (2), (4), and (5) reduce to

$$\frac{\partial^2 d_2}{\partial y^2} - \frac{d_2}{R^2} = -\frac{f^2 (z_T - h)}{g' D_1}, \quad (6)$$

where  $R$  is the Rossby radius of deformation

$$R^2 = \frac{g' \bar{D}_\infty}{f^2}, \quad \bar{D}_\infty = \frac{D_1 D_2}{D_1 + D_2}, \quad (7)$$

and  $z_T = d_1 + d_2 + h = D_1 + D_2$  is the total depth of the channel. Equation (6) gives the structure of the interfacial variations such as

$$d_2 = \frac{(d_{2+} - d_{2-}) \sinh \lambda y}{2 \sinh \lambda L/2} + \frac{(d_{2+} + d_{2-} - 2\Delta_2(z_T - h)) \cosh \lambda y}{2 \cosh \lambda L/2} + \Delta_2(z_T - h), \tag{8}$$

where  $d_{2+}$  ( $d_{2-}$ ) denotes thickness of the lower layer along the northern (southern) wall at  $y = L/2$  ( $-L/2$ ), and  $\lambda$  denotes  $R^{-1}$ . The parameter  $\Delta_2 = D_2/z_T$  is the scaled lower-layer thicknesses as  $x \rightarrow -\infty$ . Then  $d_1$  can be found from  $d_1 = z_T - d_2 - h$ . In (8),  $\Delta_2(z_T - h)$  is the thickness change of the lower layer associated with the barotropic flow riding over the sill, if baroclinic disturbances were absent. A similar solution to (8) was obtained by Pratt and Armi (1990) for a flat bottom case with coastline contractions in which the  $\Delta_2(z_T - h)$  term was not included. It is known that, with the constant PV in each layer, only internal Kelvin waves can exist along the walls where the phase speed is negative (positive) on the northern (southern) wall.

From the upper- and lower-layer momentum equations (1), Bernoulli functions yield

$$B_i = \frac{p_T}{\rho_0} + \frac{u_i^2}{2} + g' \delta_{i,2} (d_2 + h), \quad i = 1, 2$$

along the walls where  $v_i = 0$ . Further, since the streamfunctions along the wall are constant in both layers, not only the Bernoulli function of each layer but the differential Bernoulli function

$$\Delta B = B_2 - B_1 = \frac{1}{2}(u_2^2 - u_1^2) + g'(d_2 + h) \tag{9}$$

should also be conserved along the walls.

Here we consider the behavior of  $d_{2+}$  on the northern wall at  $y = L/2$  using (9). It is convenient to define an interfacial displacement  $\eta$  at the northern wall such that

$$\eta(x) = d_2 + \Delta_2(z_T - h(x)), \tag{10}$$

where the second term of the right-hand side (rhs) of (10) corresponds to the interfacial displacement by the barotropic flow. That is,  $\eta$  denotes the displacement by internal Kelvin waves, which is purely baroclinic (see Fig. 3). Then, the velocity at the wall  $y = L/2$  becomes, in terms of barotropic velocity  $u_{T+} = u_T(x, L/2)$  and the interfacial displacement  $\eta$ ,

$$u_1(x, L/2) = u_{T+} + \frac{\Delta_2 g' \lambda}{f} \eta \tag{11}$$

and

$$u_2(x, L/2) = u_{T+} - \frac{\Delta_1 g' \lambda}{f} \eta, \tag{12}$$

where  $\Delta_i = D_i/z_T$  ( $i = 1, 2$ ) is the scaled depth at  $x \rightarrow -\infty$ .

Now, coupled behavior between  $\eta(x)$  and  $u_{T+}$  may be discussed based on conservation of the differential Bernoulli function (9) and conservation of volume transport. We suppose that the Rossby radius is much smaller than the channel width, that is,  $R \ll L$ , which simplifies (8) and (9) greatly. In this case,  $d_2 - \Delta_2(z_T - h) \sim \eta(x) \exp \lambda(y - L/2)$  near the northern wall for  $R \ll L$ , representing an internal Kelvin wave structure. Further, total transport through the channel is dominated by the barotropic flow for  $R \ll L$  because transport associated with the baroclinic flow is  $O[(R/L)^2]$ . Therefore, we may view this problem as a baroclinic response of internal Kelvin waves to an imposed barotropic current as a forcing so as to conserve the differential Bernoulli function (9) along the wall. This assumption is adequate for Soya Strait where  $L \sim 50$  km and  $R \leq 10$  km.

Substituting (10), (11), and (12) into (9), we finally obtain the differential Bernoulli function such that

$$\frac{\Delta_D}{2D_\infty} \eta^2 - \left(1 - \frac{u_{T+}}{c_\infty}\right) \eta + \left[\frac{\Delta B}{g'} - (\Delta_2 z_T + \Delta_1 h)\right] = 0, \tag{13}$$

where

$$\Delta_D = \Delta_2 - \Delta_1 = \frac{D_2 - D_1}{z_T} \tag{14}$$

is the scaled depth difference between the lower and upper layer. As we will see later, this is an important parameter that determines interface behavior. In (13)  $c_\infty$  is defined by

$$c_\infty = \sqrt{g' \overline{D}_\infty}, \tag{15}$$

which is the phase speed of internal Kelvin waves in still water with depth as  $x \rightarrow \pm\infty$ .

The evolution of the internal Kelvin wave associated with the Bernoulli function is then found by substituting (11) and (12) into (1) and by taking the difference between the upper- and lower-layer momentum equations so that

$$\frac{\partial \eta}{\partial t} - c_\infty \frac{\partial}{\partial x} \left( \frac{\Delta B}{g'} \right) = 0$$

along the northern wall (where  $v_i = 0$ ). This may further yield

$$\frac{\partial \eta}{\partial t} + (u_{T+} - c_K) \frac{\partial \eta}{\partial x} = -\eta \frac{\partial u_{T+}}{\partial x} + c_\infty \Delta_1 \frac{\partial h}{\partial x}, \quad (16)$$

where

$$c_K = c_\infty \left( 1 - \frac{\Delta_D}{D_\infty} \eta \right). \quad (17)$$

Equation (16) represents internal Kelvin waves forced by barotropic flow changes and the topographic variations as in the first and second terms in its rhs, respectively. The internal Kelvin wave propagates upstream with phase speed  $-c_K$  (17) against the barotropic flow.

Equation (17) indicates that  $c_K$  depends on  $\eta$ . Further, the sign of  $\Delta_D$  is important for determining the phase speed, where  $\Delta_D$  is positive if the upper layer is thinner than the lower layer from (14). We suppose  $\Delta_D > 0$  in this paper unless otherwise specified, because this condition apparently represents a shallow seasonal thermocline in summer. With this condition,  $c_K$  decreases as  $\eta$  increases; that is, the phase speed against the flow decreases if the thin upper layer becomes thinner. This is attributed to the fact that the phase speed of the internal Kelvin wave takes the maximum value when the upper and lower layers have the same thickness. As seen in the following sections, the dependence of  $c_K$  on  $\eta$  is important for resonant generation of internal Kelvin waves and, consequently, hydraulics of the barotropic stratified flow.

### b. Control solutions

Hydraulic control occurs when the above resonant condition is realized. Characteristics of the control may be derived from (13) by defining a nondimensional functional  $J$  as follows:

$$J(F_r; x) = (1 - F_r)^2 + 2B^* - K(x), \quad (18)$$

where

$$F_r = \frac{\Delta_D}{D_\infty} \eta + \frac{u_{T+}}{c_\infty} \quad (19)$$

is a Froude number,

$$B^* = \frac{\Delta_D}{D_\infty} \left( \frac{\Delta B}{g'} - D_2 \right) \quad (20)$$

is a scaled Bernoulli constant along the wall, and

$$K(x) = \left( 1 - \frac{u_{T+}(x)}{c_\infty} \right)^2 + \frac{2\Delta_D \Delta_1 h(x)}{D_\infty}. \quad (21)$$

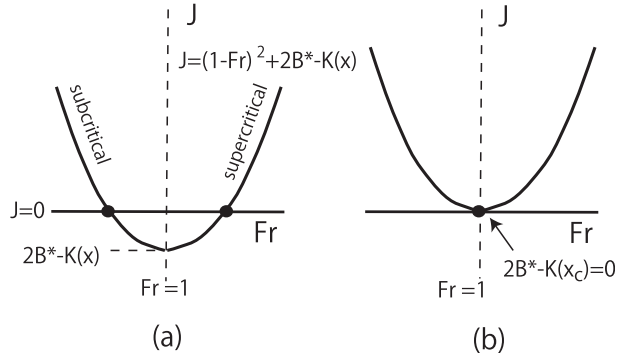


FIG. 4. Schematic plots of functional  $J$  in terms of  $Fr$  (and therefore  $\eta$ ): (a) two solutions can be obtained at  $J = 0$ , one of which is subcritical ( $Fr < 1$ ) and the other is supercritical ( $Fr > 1$ ), and (b) functional  $J$  for a critical flow case, in which the  $J$  minimum equals 0 at a critical section  $x = x_c$ ;  $x_c$  is derived from  $2B^* - K(x_c) = 0$ .

The Froude number (19) may be represented as  $Fr - 1 = (u_{T+} - c_K)/c_\infty$ , and is therefore considered as a scaled phase speed of the internal Kelvin wave.

In Eq. (18)  $J = 0$  gives two solutions with respect to  $Fr$  (and hence  $\eta$ ) as in Fig. 4a, one of which is subcritical ( $Fr < 1$ ) and the other is supercritical ( $Fr > 1$ ) if  $2B^* - K(x) < 0$ . The flow becomes critical when  $J$  minimum coincides with zero at  $Fr = 1$  (see Fig. 4b) so that the subcritical and supercritical solutions merge smoothly. The critical amplitude  $\eta_c$  should then become

$$\eta_c = \frac{\overline{D}_\infty}{\Delta_D} \left( 1 - \frac{u_{Tc}}{c_\infty} \right) \quad (22)$$

from (19), where  $u_{Tc}$  is barotropic flow at the control section. If we consider an upwelling favorable condition, as presumed above, then  $\eta_c \Delta_D > 0$ , and therefore the critical barotropic flow speed  $u_{Tc}(x)$  should be less than  $c_\infty$ .

Points of control may be derived by (21). From (13) we have  $J = 0$ , and hence

$$K(x) = (1 - F_r)^2 + 2B^*. \quad (23)$$

This indicates that  $K(x)$  should be minimum where  $Fr$  is unity because  $B^*$  is a constant (see Figs. 5a,b). This determines  $u_{Tc}$  as well as the location of the control section  $x_c$ , which in turn determines  $\eta_c$  from (22). Further, the minimum  $K$  value should be the scaled Bernoulli constant  $2B^*$ , as in (23), because  $Fr = 1$  at the control section. The shape of  $K(x)$  depends on detailed structures of  $u_{T+}(x)$  and  $h(x)$ , as well as the sign of  $\Delta_D$ . Specific numerical results will be discussed later in following sections (e.g., see Fig. 8).

Here we note some general characteristics of the control solution. As noted above,  $u_{T+}(x)$  increases as it

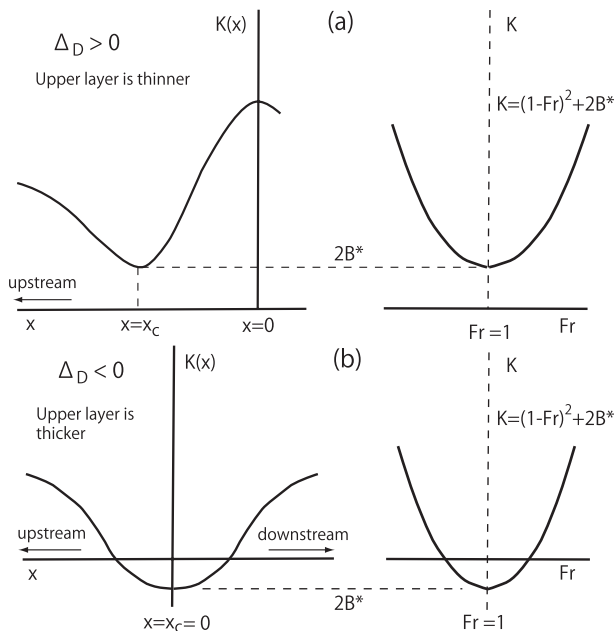


FIG. 5. Schematic plots of  $K$  for a critical flow: (left)  $K$  with respect to  $x$  [see (21)] and (right)  $K$  representing  $J = 0$  [see (23)]. Critical section occurs where  $K(x)$  is minimum, corresponding to  $Fr = 1$ . (a) Case with  $\Delta_D > 0$  in which the upper layer is thinner than the lower layer and (b) case with  $\Delta_D < 0$  in which the lower layer is thinner.

climbs up the sill. Increasing  $u_{T+}$  implies that the first term of  $K$  in the rhs of (21) is a decreasing function upstream. On the other hand, the second term (the topographic term) increases as  $x$  increases if  $\Delta_D$  is positive, that is, when the upper layer is thinner than the lower layer [see (14)]. Therefore, a control section with a  $K(x)$  minimum occurs upstream from the crest for a positive  $\Delta_D$  (see Fig. 5a). Indeed, taking the derivative of  $K$  with respect to  $x$  at the control section, we have

$$\frac{\partial K}{\partial x} = \frac{2\Delta_D}{D_\infty} \left[ -\frac{\eta_c}{c_\infty} \left( \frac{\partial u_{T+}}{\partial x} \right)_c + \Delta_1 \left( \frac{\partial h}{\partial x} \right)_c \right] = 0, \quad (24)$$

where the subscript  $c$  denotes values evaluated at the critical section. Since both  $\partial u_{T+}/\partial x$  and  $\partial h/\partial x$  are positive for  $x < 0$  and  $\eta_c$  should be positive for an upwelling situation,  $\partial K/\partial x = 0$  is realized upstream from the crest. This corresponds to the remote control discussed first in Pratt and Armi (1990).

Suppose that this upwelling situation occurs where  $\Delta_D > 0$ . In this case, the flow is subcritical for  $x < x_c$ , as in Fig. 5a, because  $c_K$  increases toward upstream direction as the upper-layer thickness is greater than that at the control section. In addition,  $u_{T+}$  is slower than  $u_{Tc}$  upstream. Both of these flow features result in  $u_{T+} - c_K < 0$  for  $x < x_c$ . On the other hand, the flow is supercritical

for  $x > x_c$  because of the reversed reason. Hence, for an upwelling situation, transition from a subcritical flow to a supercritical flow occurs smoothly at the control section where  $u_{T+} - c_K = 0$ . We will see such a remote control in numerical results in the following sections (see, e.g., Figure 8).

It should be noted that the remote control occurs only when the barotropic flow  $u_T$  is present [see (24)]. Otherwise,  $K$  has no minimum upstream.

In the case for  $\Delta_D < 0$ ,  $K(x)$  becomes minimum at  $x = 0$  because both terms in rhs of (21) take minimum values there (Fig. 5b). Therefore, the sill crest is the control section in this case, which is a conventional control solution. Further,  $\eta_c < 0$  from (22), indicating that the interface deepens as  $x$  increases. Therefore, characteristics of criticality are sensitive to the thickness ratio between the upper and lower layers, attributed to the dependence of phase speed of internal Kelvin waves on layer thickness.

In conclusion, intense upwelling occurs by nonlinear interaction between a stratified barotropic flow and a sill when the upper layer is thin like the seasonal thermocline in summer. If the interfacial displacement due to resonance becomes so large that the upper-layer thickness vanishes, that is,  $d_{1+} = 0$  or

$$\eta = \Delta_1(z_T - h), \quad (25)$$

then the cold lower-layer water outcrops at the surface.

### 3. Mechanisms of cold belt formation in a simple numerical model

#### a. Model configurations

To investigate the upwelling mechanisms discussed above and subsequent formation of the surface cold belt downstream, we conducted numerical experiments using a primitive equation ocean model. The model is formulated with the Princeton Ocean Model (e.g., Blumberg and Mellor 1987) with horizontal resolution of 5 km and 21  $\sigma$  levels. Since the internal radius is  $\sim 10$  km, this horizontal resolution does not resolve eddies. Nevertheless, the resolution was good enough for long-wave adjustment problems as seen later in this section.

The model configuration is similar to Fig. 3, where the channel is situated on a rotating frame with  $f = 10^{-4} \text{ s}^{-1}$ . The channel length is 1000 km ( $-250 \text{ km} < x < 750 \text{ km}$ ), and the width  $L$  is 120 km ( $-60 \text{ km} < y < 60 \text{ km}$ ). The channel is wide enough so that the internal Kelvin waves on one wall do not interact with those on the other wall. The wide channel configuration enables us to compare numerical results directly with the theory in section 2. A total depth  $z_T$  of 200 m is used as a standard case,

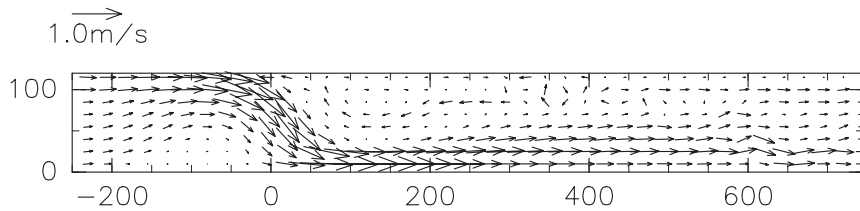


FIG. 6. Numerical result of the surface velocity field on day 30 for the inflow speed  $U_0 = 0.2 \text{ m s}^{-1}$ : sill crest located at  $x = 0$ .

although a typical vertical scale of the SWC is 100 m (see section 4b); we used somewhat deeper channels so as to show that the cold belt forms without bottom boundary layer processes as conjectured in Ishizu et al. (2006).

A Gaussian sill with a height  $h_m$  of 100 m and a half-width of 50 km is located about  $x = 0$ . Inflow (as well as initial) potential temperature distribution is

$$T(z) = 12 + 8 \tanh \xi(z - z_0), \quad (26)$$

where  $z_0$  is  $-50 \text{ m}$  and  $\xi^{-1}$  is  $50 \text{ m}$  for the standard experiment. Salinity  $S$  is set uniform in the entire domain with  $S = 33.0$ . Therefore, inflow stratification is horizontally uniform with a sharp thermocline, resembling the two-layer configuration discussed in the previous section. A uniform inflow  $u_T = U_0 = 0.2 \text{ m s}^{-1}$  is imposed at the upstream end of the channel at  $x = -250 \text{ km}$ . Baroclinic inflow is zero initially, although a radiation condition is applied for internal waves so that internal displacement is allowed at the western and eastern boundaries after adjustment by internal Kelvin waves. In conjunction with the density profile, inflow PV is uniform on isopycnal surfaces. This implies that only the internal Kelvin waves could exist, as seen in the previous section. We note, however, that horizontal viscosity is present in the numerical model, which is in fact important for PV production in the channel as we shall see later. We recall that the wall at  $y = L/2$  ( $y = -L/2$ ) was referred to as the northern (southern) wall for convenience (see Fig. 3).

*b. Coastal jet and cold belt*

Figure 6 shows a horizontal distribution of surface currents. Even though the inflow is uniform upstream, it is deformed and tends to be concentrated adjacent to the northern wall as it climbs the sill. A strong jetlike current with width  $\sim 50 \text{ km}$  occurs upstream of the crest; a boundary layer, similar to a western boundary layer of the Munk-layer type, forms against the northern wall, although in this case topographic Rossby waves on the sill slope, rather than planetary waves on a  $\beta$  plane, are responsible for forming the boundary layer (Wang and Huang 1995). The current is then separated from the

coast around the crest and deflected southward, influenced by topographic contours, retaining the jet structure. A boundary layer also forms on the southern wall downstream of the sill so that the coastal current is kept narrow and strong on the southern wall. The surface current speed achieves  $0.9 \text{ m s}^{-1}$ , which is similar to the SWC velocity.

Figure 7 shows sea surface temperature (SST) distributions on day 5, 10, and 20. A surface cold belt appears along the northern flank of the coastal jet, consistent with satellite observations (e.g., Figure 1). The cold water first appears on day 2 upstream of the sill crest. It then extends downstream along the coastal jet with time. SST becomes steady once the cold SST head passes. This behavior resembles adjustment by long waves.

A potential-temperature cross section downstream at  $x = 250 \text{ km}$  is shown in Fig. 8a. The thermocline is lifted

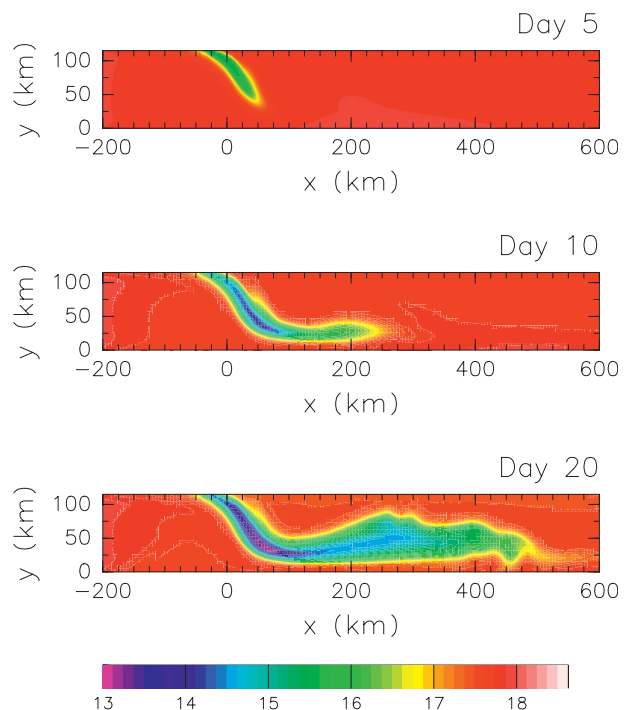


FIG. 7. SST evolution on (top) day 5, (middle) day 10, and (bottom) day 20: sill crest located at  $x = 0 \text{ km}$ .

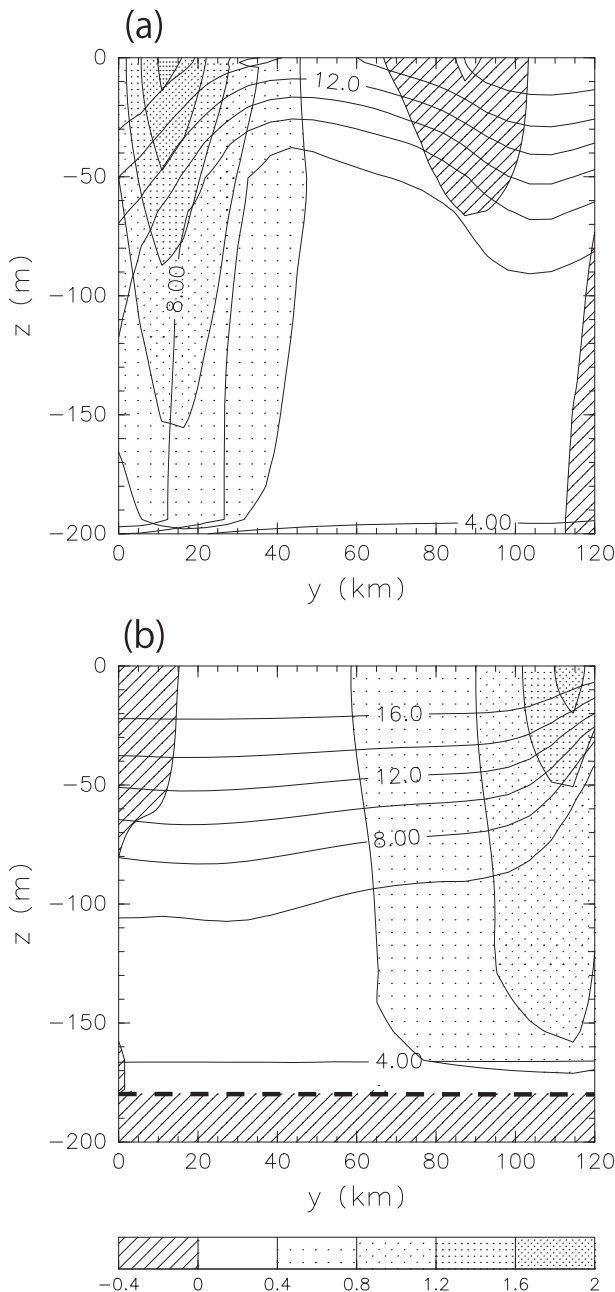


FIG. 8. (a) Cross-channel section of potential temperature (contour) and alongshore velocity (shading) at  $x = 250$  km, downstream of the sill crest: contour interval for potential temperature is  $2^{\circ}\text{C}$ , and the velocity scale is indicated at the bottom. (b) As in (a) except for the section at  $x = -110$  km, which is a location of the critical section upstream from the crest. Thick dashed line at about a depth of  $-180$  m denotes bottom on the slope.

greatly, centering around  $y = 40$  km where the cold belt forms on the surface. This doming structure corresponds well with observed temperature sections (e.g., Matsuyama et al. 2006; Ishizu et al. 2006) and those in the OGCM (Fig. 2c). The coastal current flows between the dome

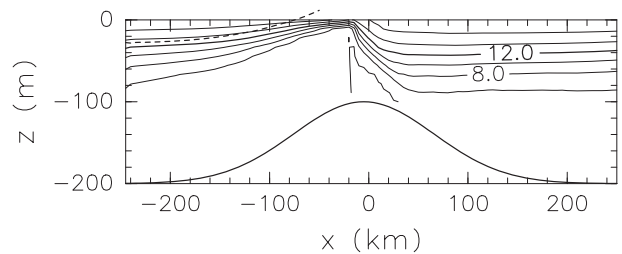


FIG. 9. Potential temperature along the northern wall at  $y = L/2$ : the  $12^{\circ}\text{C}$  contour is indicated by a thick solid line, corresponding to the interface of the two-layer model. Contour interval is  $2^{\circ}\text{C}$  and the dashed line denotes shape of the interface derived from the theoretical two-layer model based on conservation of the Bernoulli function.

and the southern coast. Isotherms are inclined there, corresponding to substantial baroclinicity in the coastal current. The  $6^{\circ}$  and  $8^{\circ}\text{C}$  contours stand even vertically. This feature can also be seen in the observations.

### c. Remote control upstream and surfacing of thermocline water

Next, we look at the response of the interface upstream. Figure 8b displays a cross-channel section of potential temperature at  $x = -110$  km. As shown later, this is a critical section in the present model setting. There is an intensified upwelling adjacent to the northern wall with a scale of the Rossby radius ( $\sim 10$  km), consistent with an internal Kelvin wave formation. Since the  $12^{\circ}\text{C}$  contour is the center of the thermocline, we may regard it as the interface of the two-layer model. The  $12^{\circ}\text{C}$  contour is lifted to a depth of 17 m toward the wall from the initial depth of 50 m. This corresponds to a stationary internal Kelvin wave.

Figure 9 displays a temperature distribution along the northern wall. The  $12^{\circ}\text{C}$  isotherm is displaced about 20 m at the inlet, indicating that the internal Kelvin wave propagates upstream and lifts the thermocline, as discussed above. The displacement of isotherms becomes greater toward the top of the sill, with the thermocline sharpened. The upper thermocline outcrops upstream of the sill crest. The isotherms then deepen rapidly downstream of the sill crest along the wall, returning to the initial depths.

Next, the nondimensional parameter  $K(x)$  is estimated by (21). The barotropic flow,  $u_T^* = u_{T+}/c_{\infty}$ , on the northern wall in (21) is derived from the numerical model as shown in Fig. 10a, where  $c_{\infty}$  is estimated by (15) with the density corresponding to the top and bottom levels; this gives  $g' = 2.45 \times 10^{-2} \text{ m s}^{-2}$  so that  $c_{\infty} = 0.96 \text{ m s}^{-1}$ . The maximum barotropic velocity in a dimensional value is  $u_{T+} = 0.81 \text{ m s}^{-1}$  at  $x = -50$  km. Correspondingly,  $u_T^*$  has a maximum value 0.84 upstream

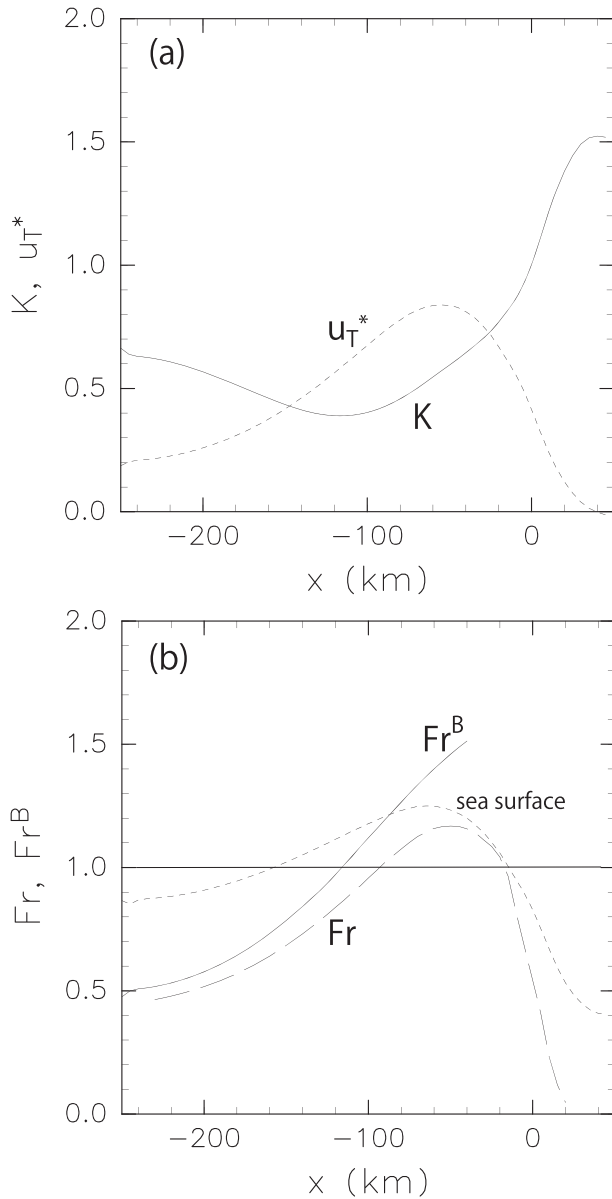


FIG. 10. Nondimensional parameters in terms of longshore position  $x$ : (a)  $u_T^*$  (dotted line) and  $K$  (solid line) and (b) the Froude number  $Fr$ , evaluated from the numerical results (long dashed line) and  $Fr^B$  derived from conservation of the Bernoulli function (solid line). The dashed line denotes  $Fr$ , derived from  $\eta$  corresponding to sea surface. Outcrop of the interface based on conservation of the Bernoulli function occurs at the intersection between  $Fr^B$  and sea surface.

from the sill crest. Note that  $u_T^*$  is smaller than unity everywhere, indicating that the critical flow would not occur unless nonlinearity due to  $\eta$  becomes large enough to reach  $\eta = \eta_c$ .

Then,  $K(x)$  is obtained by (21) using  $u_T^*$  above. It is found that  $K(x)$  becomes minimum at about  $x = -110$  km (Fig. 10a). This is a control section  $x_c$  in the present

experiment. The minimum value of  $K$  is equivalent to the scaled Bernoulli constant  $2B^*$ , as in (20), which is 0.39. As expected from (24), the control section occurs upstream from the  $u_T^*$  maximum, where both of  $u_T^*$  and  $h$  increase as  $x$  increases.

Finally, we estimate the Froude number (19) using the numerical results where the 12°C isotherm is considered as the interface of the two-layer model. In Fig. 10b,  $Fr$  is calculated directly from (19) by evaluating  $\eta$  and  $u_{T+}$  from the above numerical experiment. A theoretical estimate  $Fr^B$  using the Bernoulli function (23) is also displayed. Froude numbers  $Fr$  and  $Fr^B$  correspond well with each other, although the location of the control section in the numerical result is shifted downstream slightly. This confirms that the barotropic flow in the numerical model becomes critical with respect to the internal Kelvin wave upstream of the crest, and the interfacial displacement in this case is hydraulically controlled.

As discussed in section 2, the interfacial displacement of the two-layer model is found from the Bernoulli function (13). The interfacial displacement may be estimated theoretically by (19) and (23), which is represented by a broken line in Fig. 9. It corresponds well with the 12°C contour of the numerical result. Outcropping is estimated to occur around  $x = -85$  km according to the hydraulic theory (25), which is upstream compared with the numerical results. Nevertheless, overall structure of the interfacial displacement is well represented by the hydraulic theory.

In Fig. 10b,  $Fr$  decreases rapidly downstream from  $x = -50$  km along the coast. The barotropic flow separates from the northern coast around this position, as in Fig. 6. Therefore, the flow along the wall is no longer supercritical, and hence the internal Kelvin wave cannot propagate downstream farther. Instead, the interfacial displacement is separated from the coast together with the barotropic flow, manifesting the cold belt at the surface.

#### d. Downstream development of the cold belt

The surface cold belt was simulated well with this simple channel model (Fig. 7). Since the thermocline water outcrops to the surface, surface frontal waves may be related to formation of the downstream cold belt [cf. Gill and Schumann (1979) and Dale and Barth (2001) for a two-layer model with zero PV, or infinitely deep, lower-layer inflow]. It is not obvious, however, whether the surface frontal wave would always propagate following the barotropic current like the cold belt along the SWC.

To understand propagation characteristics of the interfacial displacement, it is instructive to consider a deep-channel case in which the thermocline does not outcrop

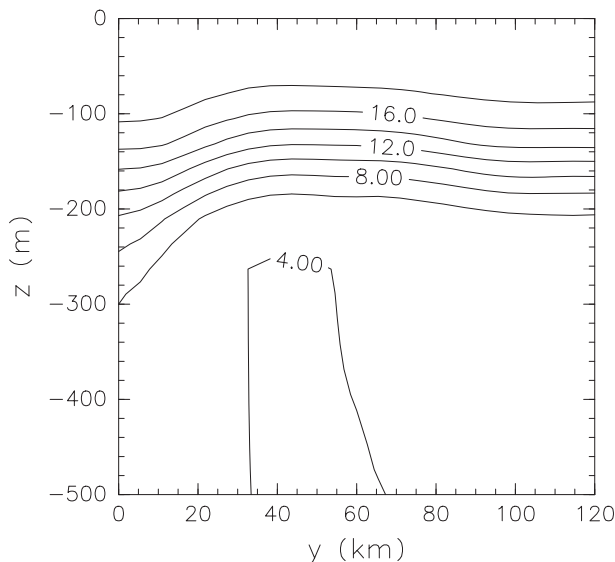


FIG. 11. Cross-channel section of potential temperature at  $x = 250$  km for the deep-channel case, contour interval  $2^\circ\text{C}$ .

to the surface, where the surface frontal waves are absent. We conducted a numerical experiment with  $z_T = 500$  m. The cross-channel temperature section shows that, even though the channel is deep, we can see a lifted thermocline at around 40 km from the southern coast on the northern flank of the coastal current (Fig. 11). This seems somewhat puzzling on first glance because the inflow should have uniform PV and, therefore, it would not support any waves interior of the channel except for internal Kelvin waves along the walls.

The top panel of Fig. 12 displays barotropic PV distribution of the depth-averaged flow to understand propagation of the upwelling signal in the interior of the channel. It was found that intensive barotropic PV production occurs in a boundary layer along the northern wall upstream of the sill crest associated with the coastal jet. The coastal jet then separates from the northern wall around the crest, accompanying the high PV region associated with the current shear along the northern flank of the barotropic flow. Such a strong shear zone can also be seen in the SWC on its northern flank (Matsuyama et al. 2006).

This results in breaking uniformity in the PV distribution, implying that a waveguide forms in the interior of the channel. That is, vorticity waves can propagate along this waveguide.

The bottom panel of Fig. 12 shows a displacement of the  $12^\circ\text{C}$  isotherm for the deep-channel case. The effects of the barotropic flow on the interfacial displacement,  $\Delta_2(z_T - h)$ , is removed from the second-layer thickness so that a purely baroclinic response  $\eta$  can be seen. Comparing between the top and bottom panels of Fig. 12, the interface and its head propagates along the barotropic flow

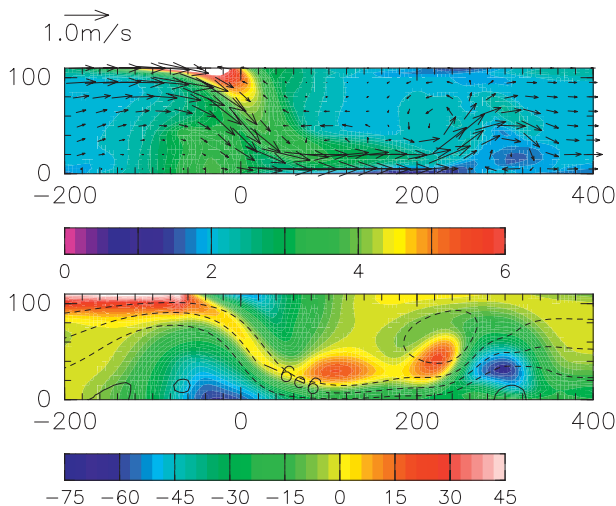


FIG. 12. (top) Barotropic potential vorticity  $\times 10^7$  (color shading) and barotropic velocity field (vectors) in the deep-channel case at day 10 and (bottom) the  $12^\circ\text{C}$  isotherm interface displacement (color shading) and geostrophic contours in the deep-channel case.

where the PV gradient is high. This indicates that the subsurface doming structure is produced by propagation of baroclinic vorticity waves along the barotropic current shear, which carries the upwelling signal caused by resonance.

We consider this baroclinic adjustment problem using a two-layer quasi-geostrophic equation because the downstream shoaling should be formed by vorticity waves in a deep channel. The same model geometry and nomenclature as those in Fig. 3 in section 2 are used here, although  $|h/z_T| \ll 1$ ,  $|h/D_2| \ll 1$ , and  $|\eta/z_T| \ll 1$  are assumed for quasi-geostrophy. Potential vorticity in terms of the barotropic and baroclinic components is, respectively,

$$q_T = \nabla^2 \psi_T + \frac{fh}{z_T}; \quad q_c = \nabla^2 \psi_c - \frac{\psi_c}{R^2}, \quad (27)$$

where  $\psi_T$  and  $\psi_c$  are barotropic and baroclinic streamfunctions, such that

$$\psi_T = \frac{1}{\rho_0 f z_T} (D_1 p_1 + D_2 p_2);$$

$$\psi_c = \frac{1}{\rho_0 f} (p_2 - p_1) = \frac{g'}{f} (d_2 + h - D_2). \quad (28)$$

Note that  $\psi_c$  represents interfacial displacement as seen in (10).

As soon as a barotropic flow is imposed upstream, the barotropic jet is produced downstream quickly. Therefore, barotropic streamfunction  $\psi_T$  is considered as a given function for the baroclinic adjustment problem. Cross-PV-front scale of the interfacial displacement,

represented by  $\psi_c$ , should scale with the barotropic current width  $L_B$  because the vorticity wave is supported by the PV gradient of the barotropic current. It is instructive to suppose a case with  $|R^2/L_B^2| \ll 1$  first. This yields  $\nabla^2 \psi_c \ll \psi_c/R^2$  in  $q_c$ . Then the baroclinic PV equation is reduced to

$$\frac{\partial q_c}{\partial t} + J(Q, q_c) + J\left(\psi_T, \frac{fh}{D_2}\right) = 0, \quad (29)$$

where  $J(a, b)$  is the Jacobian and

$$Q = \psi_T + R^2 \left( \nabla^2 \psi_T + \frac{D_1}{D_2} \frac{fh}{z_T} \right)$$

represents baroclinic wave characteristics, called the geostrophic contours (Pedlosky 1996), along which baroclinic waves propagate with a phase speed

$$c = \tilde{u}_T + R^2 \frac{\partial^2 \tilde{u}_T}{\partial \tilde{y}^2} - \frac{g' \Delta_1}{f} \frac{\partial h}{\partial \tilde{y}}. \quad (30)$$

Here  $\tilde{u}_T$  denotes the barotropic flow in the  $Q$ -contour direction, and  $\tilde{y}$  is the coordinate normal to the  $Q$  contour. The first term in the rhs of (30) represents advection by barotropic flow in the downstream direction. The second term characterizes upstream propagation of the vorticity wave associated with shear of the barotropic jet along the current axis, although this is a small term if  $|R^2/L_B^2| \ll 1$  is assumed. The third term characterizes propagation as a topographic Rossby wave; if there were shelf-slope topography along the southern wall, as the coast off Hokkaido, the topographic Rossby wave term would contribute to downstream propagation. Note that the topographic effects decrease as the upper layer becomes thinner.

As far as  $|R^2/L_B^2| \ll 1$  is assumed, the advective term is dominant in (30) and, therefore, the baroclinic signal propagates downstream along the current axis because  $Q$  is parallel mostly to  $\psi_T$ . In general,  $|R^2/L_B^2|$  may be  $O(1)$ . In this case, the PV equation may be reduced to an eigenvalue problem in which  $c$  is an eigenvalue. Nevertheless, (30) should be qualitatively applicable although the phase speed of the vorticity wave against the current, corresponding to the second term in (30), is now comparable to the barotropic current speed. Figure 12 (bottom) shows that the interfacial displacement in the deep-channel case, in which the  $Q$  contours evaluated from the numerical results are superimposed. As expected, the interfacial displacement is mostly parallel to the  $Q$  contours. This indicates that baroclinic adjustment occurs along the axis of the barotropic current, resulting in producing a subsurface doming structure downstream from the sill.

It was observed that the SWC has strong baroclinicity at its axis (Matsuyama et al. 2006; Fukamachi et al. 2008; see also a simulation result of Fig. 3). This is consistent with the baroclinic adjustment mechanism by vorticity waves along the barotropic jet axis.

## 4. Discussion

### a. Flow criticality

Here we consider conditions in which the controlled solutions are established. Suppose that a barotropic flow (without interfacial displacements) is present initially in a flat bottom channel, and then a sill is introduced suddenly (see, e.g., section 1.6 of Pratt and Whitehead 2008). In this case, unless the flow is critical, it usually generates forced disturbances locally around topography so that upstream influences would not appear except for free waves. If there are no upstream influences in which  $\eta = 0$  as  $x \rightarrow -\infty$ , then  $2B^* = [K - (1 - F_r)^2]_{x \rightarrow -\infty} = 0$  from (19), (20), and (23) in conjunction with  $h \rightarrow 0$  far upstream. Hence we obtain, from the conservation of differential Bernoulli function,

$$K(x) - (1 - F_r)^2 = 0 \quad (31)$$

everywhere along the wall as far as  $\eta = 0$  as  $x \rightarrow -\infty$ . If the sill height approaches a critical condition so that  $F_r \rightarrow 1$ , (31) is valid as far as

$$K \rightarrow K(x_c) = \frac{2\Delta_D \Delta_1 h_c}{D_\infty} + \left(1 - \frac{u_{Tc}}{c_\infty}\right)^2 > 0. \quad (32)$$

In other words, once  $K(x_c) < 0$  at  $F_r = 1$ , (31) no more holds, so  $2B^* = K(x_c)$  cannot be zero but negative. This implies that an upstream elevation  $\eta_{-\infty}$  occurs as far as  $K(x_c) = 2B^* < 0$ , where

$$\frac{\Delta_D}{D_\infty} \eta_{-\infty} = \left(1 - \frac{u_{Tc}}{c_\infty}\right) - \sqrt{\left(1 - \frac{u_{Tc}}{c_\infty}\right)^2 - 2B^*} \quad (33)$$

as  $x \rightarrow -\infty$ .

Let us consider a case with  $\Delta_D < 0$ , first, in which the lower layer is thinner than the upper layer. In this case, considering (32), a critical flow with the upstream influences (33) occurs if

$$1 - \frac{u_{Tc}}{c_\infty} < \sqrt{\frac{2|\Delta_D \Delta_1 h_c}{D_\infty}},$$

where the control section occurs at the sill crest. That is, for a given sill height, the critical flow is realized if

detuning from exact resonance,  $|c_\infty - u_{Tc}|$ , is sufficiently small (e.g., Grimshaw and Smyth 1986). Since the control section for the  $\Delta_D < 0$  case occurs around the sill crest, as discussed in section 2, this is a conventional resonance condition of a flow over topography controlled at the crest.

Next, we consider a case with  $\Delta_D > 0$  in which the upper layer is thinner. Contrary to the previous case, (32) indicates that  $K(x) > 0$  is always realized as far as  $h$  is positive. Therefore, a solution  $\eta = 0$  as  $x \rightarrow -\infty$  with  $B^* = 0$  (i.e., noncritical flow) can always occur irrespective of the sill height and the inflow  $U$ . On the other hand, we have shown in the previous sections that the critical flow with  $F_r = 1$  is realized even for the  $\Delta_D > 0$  condition. Upstream interface elevation  $\eta = \eta_\infty$  is represented by (33), although  $B^* = K(x_c)/2$  is positive in this case. Therefore, this suggests that the two solutions, which are related to  $\eta = 0$  and  $\eta = \eta_\infty$  as  $x \rightarrow -\infty$ , could exist for given  $h(x)$  and  $U_0$ . That is, multiple equilibria might occur.

To observe criticality of the flow with  $\Delta_D > 0$ , we first conducted numerical experiments with various inflow speed  $U_0$ . Figure 13a shows  $K(x)$  obtained numerically. This shows that the minimum value of  $K$ , that is,  $K(x_c) = 2B^*$ , increases with decreasing  $U_0$ . The position of  $K$  minimum does not move significantly as  $U_0$  varies. This suggests that, as far as conservation of the Bernoulli function is applicable,  $x_c$  would not move greatly with  $U_0$ .

Then, Fig. 13b shows  $F_r$  calculated directly from (19) for various  $U_0$  by evaluating  $\eta$  and  $u_{T+}$  from numerical experiments. Another Froude number estimate,  $F_r^B$  based on conservation of the Bernoulli function (23), is also displayed. Only  $F_r^B$  with  $U_0 = 0.3 \text{ m s}^{-1}$  is displayed; the other cases give similar  $F_r^B$  because the position of  $K$  minimum does not move greatly as  $U_0$  changes.

As seen in Fig. 13b,  $F_r$  and  $F_r^B$  show excellent correspondence with each other for high inflow speed such as  $U_0 = 0.3 \text{ m s}^{-1}$ . The critical section where  $F_r = 1$  is located at  $x = -110 \text{ km}$ , which corresponds well with the position of the  $K$  minimum (or  $F_r^B = 1$ ).

As the inflow speed decreases, however, the control section with  $F_r = 1$  moves downstream from the location of the  $K$  minimum toward the sill crest. This is not expected with conservation of the Bernoulli function because the  $K$  minimum position does not move much with  $U_0$  as in Fig. 13a. Therefore, conservation of the Bernoulli function, or baroclinic energy, along the wall may be violated when the barotropic flow is slow. Friction could be important for the downstream migration of the critical section (e.g., section 1.9 of Pratt and Whitehead 2008).

Figure 13b also indicates that the maximum of  $F_r$  decreases with decreasing  $U_0$ . The maximum  $F_r$  becomes less than unity for  $U_0 < 0.1 \text{ m s}^{-1}$  and, hence, the flow

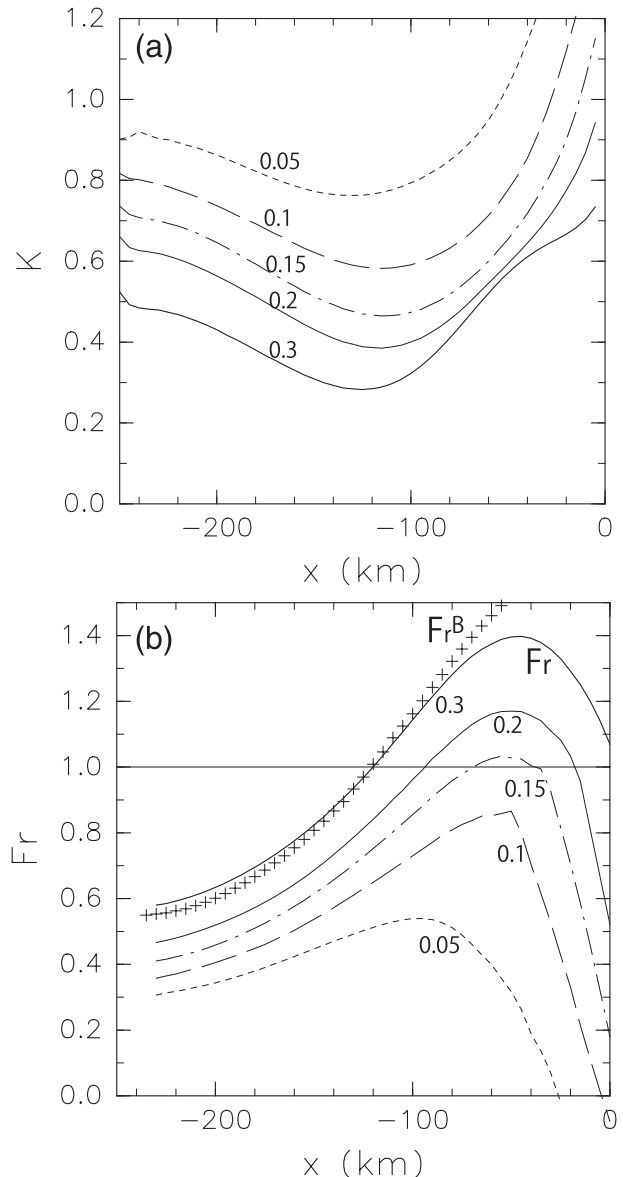


FIG. 13. (a)  $K(x)$  for various inflow derived from the numerical experiments for  $U_0 = 0.3$  (thick solid line),  $0.2$  (thin solid line),  $0.15$  (dashed/dotted line),  $0.1$  (dashed line), and  $0.05 \text{ m s}^{-1}$  (dotted line). Numbers close to the lines denote  $U_0$ . (b)  $F_r(x)$  from the numerical experiments for various inflow  $U_0$ ; crosses represents  $F_r^B$  with  $U_0 = 0.3 \text{ m s}^{-1}$  in which conservation of the Bernoulli function is assumed.

becomes subcritical. In the  $U_0 = 0.05 \text{ m s}^{-1}$  case, we also note that the position of maximum  $F_r$  moves upstream and approaches to the  $K$  minimum position.

Next, we examined the transition from subcritical flow to critical flow. To do this, the inflow speed is gradually and slowly increased in time such that

$$U_0 = 2.0 \times \text{days m s}^{-1};$$

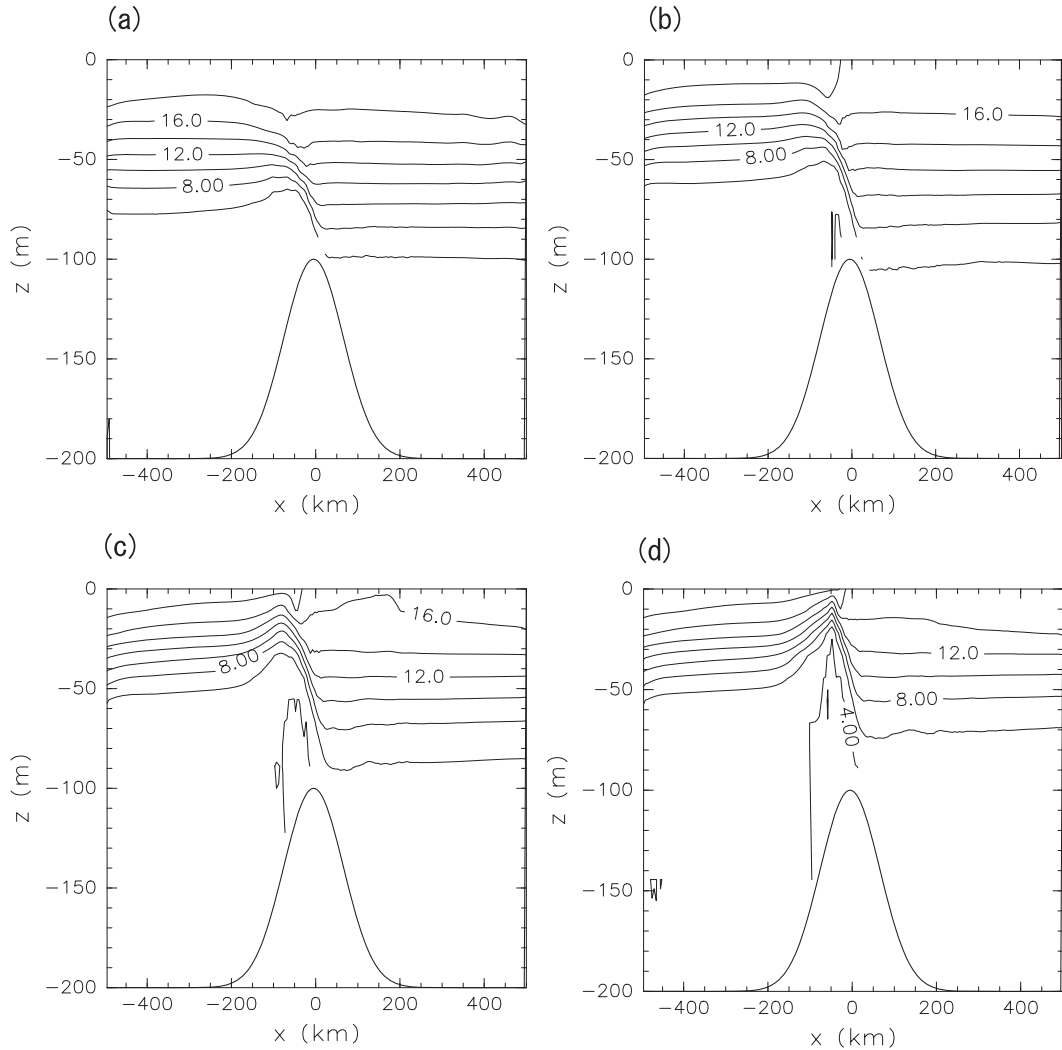


FIG. 14. Interfacial displacement along the northern wall in a numerical experiment using a channel model. The inflow is gradually increasing from  $U_0 = 0$  to  $0.2 \text{ m s}^{-1}$  in 1000 days: (a)  $U_0 = 0.04$ , (b)  $U_0 = 0.08$ , (c)  $U_0 = 0.12$ , and (d)  $U_0 = 0.16 \text{ m s}^{-1}$ .

that is, the inflow becomes  $0.2 \text{ m}^{-1}$  in 1000 days—the flow should be almost in equilibrium instantaneously. Initially, the stratification is undisturbed and inflow speed is zero so that the flow is subcritical. Therefore, it was conjectured that this would be a subcritical branch, and no upstream interfacial elevation would occur even if  $U_0$  is increased.

Unexpectedly, however, the upstream elevation of interface occurs even with small  $U_0$ , such as  $U_0 = 0.04$  and  $0.08 \text{ m s}^{-1}$ , when the flow is completely subcritical (Figs. 14a,b). Because of this upstream elevation (i.e.,  $\eta_{-\infty} > 0$ ),  $B^*$  evaluated by (33) is nonzero even for these subcritical flows.

The critical flow occurs when the  $K$  minimum becomes sufficiently small so that  $K(x_c) - 2B^* = 0$  at the

control section. Upwelling upstream of the sill crest emerges with  $U_0 = 1.2 \text{ m s}^{-1}$  when the flow apparently encounters this critical flow condition (see Fig. 14c). The upwelling further develops with  $U_0 = 1.6 \text{ m s}^{-1}$  (Fig. 14d).

Contrary to the initial assumption in this section, the upstream elevation of the thermocline occurs even when the flow is completely subcritical. The upstream elevation determines  $B^*$ , which is not zero even for a subcritical flow in this case. Therefore, the subcritical branch connects smoothly to the critical-flow branch as the inflow speed increases. It is not yet understood why the upstream elevation occurs for the subcritical flow, and multiple equilibria are not seen in the parameter range investigated here. Further studies to identify detailed characteristics of the solutions are necessary.

### b. Soya Warm Current in GCM

The channel model above represents characteristics of the cold belt well, which is seen in the GCM described in section 1. In the GCM, a strong upwelling is observed at the southwestern coast of Sakhalin Island, consistent with the theoretical as well as the channel model results. In conjunction with the internal Kelvin wave structure near the coast in Fig. 2c, upwelling is likely to be caused by the hydraulic control mechanism pursued in the present paper. Soya Strait is about 50 km, which gives a typical cross-stream scale for the barotropic current of the real SWC. Since  $R < 10$  km for Soya Strait, the assumption  $L \gg R$  is reasonable there. Therefore, the hydraulic theory in this study should be applicable.

Further, the downstream development of the cold belt and the subsurface doming structure are represented along the SWC axis in the GCM, which implies the baroclinic adjustment mechanism, as discussed in section 3. Therefore, the cold belt formation and subsurface doming in the GCM is explained well with the present theory.

Let us estimate the nondimensional parameters associated with the upwelling in the GCM. The depth of the seasonal thermocline is about 30 m, which is  $D_1$  as in Fig. 2b. The baroclinic motion, where the depth-integrated flow is removed, can be seen up to 100 m (Fig. 15), so  $z_T$  is considered as 100 m and  $D_2 = 70$  m. Then  $\bar{D}_\infty = 21$  m and  $c_\infty = 0.72$  m s<sup>-1</sup>, where the density difference between the upper and lower layers is the same as that in the previous section. From Fig. 2a,  $u_{T+} = 0.6$  m s<sup>-1</sup> and  $\eta = 20$  m at least. The Froude number is estimated as

$$F_r = \frac{u_{T+}}{c_\infty} + \Delta_D \frac{\eta}{\bar{D}_\infty} \approx 1.3.$$

Therefore, the Froude number of the GCM exceeds unity as expected at the southern portion of Sakhalin Island. This indicates that the control section should occur upstream along the coast.

In the present model, a flat bottom with a sill was considered as the bottom topography. In reality and in the GCM, the continental shelf and slope is present along the coast, which allows adjustment of the barotropic flow to occur via continental shelf waves (Ohshima 1994). This implies that the PV structure may be quite different from those of the present channel model. Nevertheless, the baroclinic waves tend to follow the barotropic current shear rather than topography if the upper layer is thin [see (30)]. As in the channel model, the cold belt is formed along the axis of the SWC in the GCM, where a strong shear zone is present (see Fig. 2a).

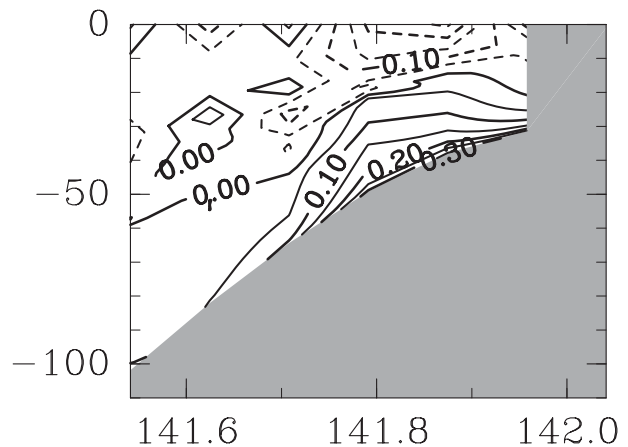


FIG. 15. Baroclinic velocity field off Sakhalin in which depth-averaged flow is subtracted from the total flow field.

Therefore, the formation mechanism of the cold belt in the GCM does not change essentially from our discussion pursued in this paper.

Seasonal variations in SWC transport are caused mainly by the pressure gradient between the Japan Sea and Sea of Okhotsk, which is caused by alongshore wind in the Sea of Okhotsk (Tsujino et al. 2008). As discussed in this paper, the upwelling and cold belt formation on a seasonal time scale is, we believe, forced by the barotropic flow of the SWC response to this pressure gradient. One might suspect that local wind stress could also cause upwelling along the southern Sakhalin coast if the wind is northeasterly. With respect to mean winds in this region, it is weak ( $< 0.01$  N m<sup>-2</sup>) in summer and, therefore, the upwelling formation on the seasonal time scale is not likely to be driven by wind. On the other hand, there are strong variations in SWC velocity with a period of 5 ~ 20 days, responding to synoptic wind stress fields (Ebuchi et al. 2009). Baroclinic response to wind on this time scale should be studied in the future.

## 5. Conclusions

We have investigated the formation mechanisms of the surface cold belt offshore of the Soya warm current (SWC). First, we showed the result of a simulation using an ocean circulation model with realistic configurations to extract dynamical essences. The model captures characteristics of the surface cold belt and the subsurface doming structure very well. Next, simple numerical model experiments were conducted and the results were discussed from the point of view of hydraulic control theory. It has been shown that there are two important mechanisms incorporated in the formation of the surface cold belt:

- Strong upwelling takes place on the southwestern tip of Sakhalin Island when the SWC flows over the shallow Soya Strait. Numerical experiments with the simple model indicated that hydraulic control of the barotropic stratified flow over topography, through internal Kelvin waves, is essential to generate the strong upwelling upstream of the shallow Soya Strait.
- The upwelling signal at Soya Strait propagates farther downstream along the waveguide associated with the vorticity front offshore of the SWC, forming a subsurface doming structure. The thermocline water outcrops to the surface and forms the surface cold belt above the subsurface dome.

It was also found that, in addition to a shallow bottom topographic feature, a shallow thermocline is dynamically important for the upwelling to occur. In this case, the control section is not located at the sill crest, but is located upstream remotely. The SWC in summer is suitable for the upwelling because the seasonal thermocline is shallow and the flow through the strait is strongest.

A main purpose of this study is to show that the cold belt is formed by the hydraulic mechanisms. Therefore, relatively deep channels (200-m and 500-m depths) were used in the idealized numerical model so that numerical results would not be influenced greatly by the bottom boundary layer. The SWC flows over a shallow continental shelf about 50–150 m deep, and bottom boundary layer may possibly cause three-dimensional flow structure, including vertical velocity. Ishizu et al. (2006) conjectured that the cold belt might be generated by upwelling from the bottom Ekman layer in which convergence occurs between the nearshore strong bottom flow of the SWC and the offshore quiet shelf water. We suspect that this would hardly occur for a stratified flow over a slope because bottom boundary layer transport and associated vertical circulation tend to be shut down by the thermal wind relation at the top of the boundary layer (Chapman 2002). Nevertheless, quantitative evaluation of the bottom boundary layer and vertical circulation should be examined further to clarify the relative importance between hydraulic effects and bottom boundary effects on the cold belt formation.

The remote control by topography and the associated upwelling is an interesting character of barotropic stratified flows. Although this has not been applied widely to oceanic phenomena so far, there may be broad applicability of this mechanism to flows through straits. For example, Tsugaru Strait, located between Hokkaido and Honshu in Japan (see Fig. 1b), exhibits a similar upwelling structure on the northern coast (Nakajima et al. 2008). Further, this mechanism may also be applicable to surface front genesis of the strong jets. The Kuroshio

surface current is accelerated sharply and frontogenesis occurs when it passes capes along Japan (T. Miyama and Y. Miyazawa 2010, personal communication). In this respect, this study is similar to studies of the Agulhas Current by Gill and Schumann (1979) and a coastal upwelling by Dale and Barth (2001), although here the depth-averaged barotropic current was considered explicitly, while in their studies an infinitely deep (or zero PV) lower layer was assumed. We believe that the present theory would give a broad basis for studies on baroclinic response of a flow over topography in which the barotropic (net depth averaged) flow component is significant.

*Acknowledgments.* We enjoyed discussions with Dr. T. Motoi, Dr. T. Miyama, Dr. I. Tanaka, and Prof. K. I. Ohshima. Ms. S. Abe is thanked for preparation of some figures. Comments from reviewers and the editor improved this paper greatly. This work was supported by NEDO Grant 07E52009a. Numerical calculations were conducted with the Pan-Okhotsk Information System, and the figures were prepared by GFD Dennou Library.

#### REFERENCES

- Blumberg, A. F., and G. L. Mellor, 1987: A description of a three-dimensional coastal ocean circulation model. *Three-Dimensional Coastal Ocean Models*, N. Heaps, Ed., Vol. 4, *Coastal and Estuarine Sciences*, American Geophysical Union, 1–16.
- Chapman, D. C., 2002: Deceleration of a finite-width, stratified current over a sloping bottom: Frictional spin-down or buoyancy shutdown? *J. Phys. Oceanogr.*, **32**, 336–352.
- Dale, A. C., and J. A. Barth, 2001: The hydraulics of an evolving upwelling jet flowing around a cape. *J. Phys. Oceanogr.*, **31**, 226–243.
- Ebuchi, N., Y. Fukamachi, K. I. Ohshima, K. Shirasawa, M. Ishikawa, T. Takatsuka, T. Daibou, and M. Wakatsuchi, 2006: Observation of the Soya Warm Current using HF ocean radar. *J. Oceanogr.*, **62**, 47–61.
- , —, —, and M. Wakatsuchi, 2009: Subinertial and seasonal variations in the Soya Warm Current revealed by HF ocean radars, coastal tide gauges, and bottom-mounted ADCP. *J. Oceanogr.*, **65**, 31–43.
- Fukamachi, Y., I. Tanaka, K. I. Ohshima, N. Ebuchi, G. Mizuta, H. Yoshida, S. Takayanagi, and M. Wakatsuchi, 2008: Volume transport of the Soya Warm Current revealed by bottom-mounted ADCP and ocean-radar measurement. *J. Oceanogr.*, **64**, 385–392.
- Gill, A. E., and E. H. Schumann, 1979: Topographically induced changes in the structure of an inertial coastal jet: Application to the Agulhas Current. *J. Phys. Oceanogr.*, **9**, 975–991.
- Grimshaw, R. H. J., and N. Smyth, 1986: Resonant flow of a stratified fluid over topography. *J. Fluid Mech.*, **169**, 429–464.
- Ishizu, M., Y. Kitade, and M. Matsuyama, 2006: Formation mechanism of the cold-water belt formed off the Soya Warm Current. *J. Oceanogr.*, **62**, 457–471.
- Matsuyama, M., M. Wadaka, T. Abe, M. Aota, and Y. Koike, 2006: Current structure and volume transport of the Soya Warm Current in summer. *J. Oceanogr.*, **62**, 197–205.

- Mellor, G. L., S. Häkkinen, T. Ezer, and R. Patchen, 2002: A generalization of a sigma coordinate ocean model and an intercomparison of model vertical grids. *Ocean Forecasting: Conceptual Basis and Applications*, N. Pinardi and J. D. Woods, Eds., Springer, 55–72.
- Miyazawa, Y., and Coauthors, 2008: Water mass variability in the western North Pacific detected in a 15-Year eddy resolving ocean reanalysis. *J. Oceanogr.*, **65**, 737–756.
- Mustapha, M. A., S. Saitoh, and T. Lihan, 2009: Satellite-measured seasonal variations in primary production in the scallop-farming region of the Okhotsk Sea. *J. Mar. Sci.*, **66**, 1557–1569.
- Nakajima, Y., and Coauthors, 2008: Tsugaru warm current water inflow to Tsugaru Strait (in Japanese with English abstract and figure captions). *Umi Sora*, **84**, 1–16.
- Nakata, A., I. Tanaka, H. Yagi, G. Kantakov, and A. Samatov, 1996: Origin of water in the Cold Water Belt appearing offshore side of the Soya Warm Current near La Perouse Strait (the Soya Strait). *Extended Abstracts, Fifth PICES Annual Meeting*, Nanaimo, Canada, PICES, 11–20.
- Ohshima, K. I., 1994: The flow system in the Japan Sea caused by a sea-level difference through shallow straits. *J. Geophys. Res.*, **99**, 9925–9940.
- Pedlosky, J., 1996: *Ocean Circulation Theory*. Springer, 453 pp.
- Pratt, L., and L. Armi, 1990: Two-layer rotating hydraulics: Strangulation, remote and virtual controls. *Pure Appl. Geophys.*, **133**, 587–617.
- , and J. A. Whitehead, 2008: *Rotating Hydraulics: Nonlinear Topographic Effects in the Ocean and Atmosphere*. Springer, 589 pp.
- Tsujino, H., H. Nakano, and T. Motoi, 2008: Mechanism of currents through the straits of the Japan Sea: Mean state and seasonal variation. *J. Oceanogr.*, **64**, 141–161.
- Uchimoto, K., H. Mitsudera, N. Ebuchi, and Y. Miyazawa, 2007: Anticyclonic eddy caused by the Soya Warm Current in an Okhotsk OGCM. *J. Oceanogr.*, **63**, 379–391.
- Wang, L., and R. X. Huang, 1995: A linear homogeneous model of wind-driven circulation in a  $\beta$ -plane channel. *J. Phys. Oceanogr.*, **25**, 587–603.